# Photoisomerization of Silyl-Substituted Cyclobutadiene Induced by $\sigma \rightarrow \pi^*$ Excitation: A Computational Study

Zexing Qu, Chen Yang, and Chungen Liu*

Institute of Theoretical and Computational Chemistry, Key Laboratory of Mesoscopic Chemistry of the Ministry of Education (MOE), School of Chemistry and Chemical Engineering, Nanjing University, Nanjing 210093, China

S *Supporting Information*

ABSTRACT: Photoinduced chemical processes upon Franck−Condon (FC) excitation in tetrakis(trimethylsilyl)-cyclobutadiene (TMS-CBD) have been investigated through the exploration of potential energy surface crossings among several low-lying excited states using the complete active space self-consistent field (CASSCF) method. Vertical excitation energies are also computed with the equation-of-motion coupled-cluster model with single and double excitations (EOM-CCSD) as well as the multireference Møller−Plesset (MRMP) methods. Upon finding an excellent coincidence between the computational results and experimental observations, it is suggested that the Franck−Condon excited state does not correspond to the first $\pi-\pi^*$ single excitation state

(S_1, 1^1B_1 state in terms of D_2 symmetry), but to the second $^1B_1$ state (S_3), which is characterized as a $\sigma-\pi^*$ single excitation state. Starting from the Franck−Condon region, a series of conical intersections (CIs) are located along one isomerization channel and one dissociation channel. Through the isomerization channel, TMS-CBD is transformed to tetrakis(trimethylsilyl)-tetrahedrane (TMS-THD), and this isomerization process could take place by passing through a "tetra form" conical intersection. On the other hand, the dissociation channel yielding two bis(trimethylsilyl)-acetylene (TMS-Ac) molecules through further stretching of the longer C−C bonds might be more competitive than the isomerization channel after excitation into S_3 state. This mechanistic picture is in good agreement with recently reported experimental observations.
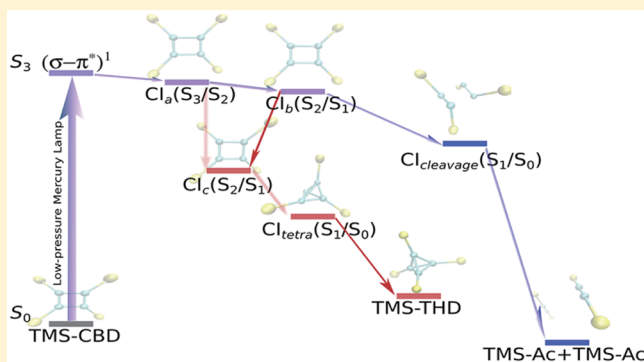
INTRODUCTION

Ring-strained organic molecules, such as cyclobutadiene (CBD) or tetrahedrane (THD), where the C−C−C bond angles deviate substantially from the ideal sp^2 or sp^3 values, respectively, have generated considerable interest from both experimental and theoretical chemists over the past half century[1−10] because of not only their abnormal bonding properties of general scientific importance but also the possible applications arising from their extraordinary electronic behaviors.[11−13]

Although the unsubstituted CBD and THD molecules are highly unstable, many of their substituted derivatives have been synthesized, showing unexpected thermal stability at or even highly above room temperatures.[14−19] Further studies revealed that interesting photo and thermoisomerizations could take place between CBD and THD frameworks.[17,18,20−23] For instance, tetrakis(trimethylsilyl)-cyclobutadiene (TMS-CBD), which has been successfully synthesized and fully characterized, is a superior photochemical precursor for tetrakis(trimethylsilyl)-tetrahedrane (TMS-THD).[18] Although thermal rearrangement from CBD to THD is symmetry-forbidden, this isomerization process could be initiated by light irradiation.[23,24] Unfortunately, this reaction channel is severely obstructed by a competitive dissociation path yielding two bis(trimethylsily)-acetylene (TMS-Ac) molecules, as shown in Scheme 1. So far, the only

Scheme 1

$-TMS \equiv Trimethylsilyl$
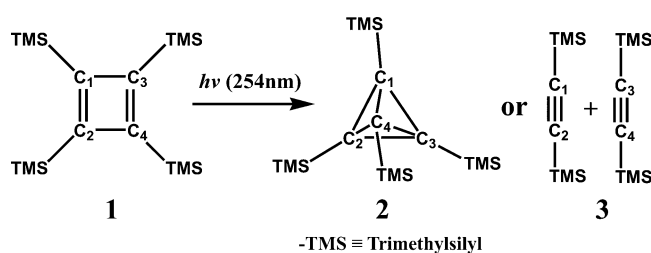
reported successful synthesis was implemented at an extremely low temperature of −130 °C, upon a sustained very long time irradiation using a low-pressure mercury lamp (254 nm).[18]

Theoretically, irradiation-initiated conversion from CBD to THD has also been studied recently, which followed the $S_1 \rightarrow S_0$ transition path through a tetra-radical form conical intersection (CI$_{tetra}$).[24−26] Franck−Condon (FC) excitation was assigned to the S_1 state, which is attributed to 1^1B_1 state (in terms of D_2 symmetry), corresponding to a $\pi \rightarrow \pi^*$ single excitation.
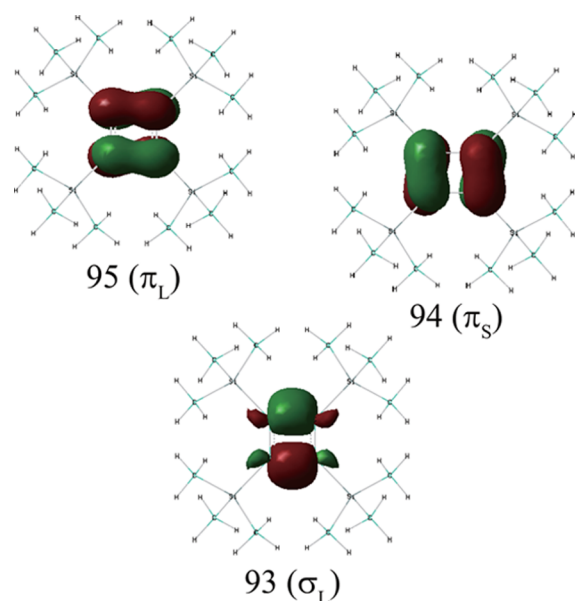
State	Configuration	f
S_0 (GS)	82.4% $(94)^2(95)^0$	-
S_1	86.1% $(94)^1(95)^1$	0.00056
S_2	76.0% $(94)^0(95)^2$	-
S_3	81.8% $(93)^1(95)^1$	0.00154

Figure 1. Illustration of the three most active natural orbitals involved in the description of the low-lying excited states, which are computed with the ground state geometry. The subscripts "S" and "L" indicate the natural orbitals located on shorter and longer C−C bonds, respectively. The major electronic configurations as well as oscillator strengths (f) are computed at the CASSCF(12,12)/6-31G(d) level.

However, near CI_{tetra} point, S_1 is characterized as a $\pi \rightarrow \pi^*$ double excitation state (2^1A state at FC point), which implies that there should exist a crossing between 1^1B_1 and 2^1A states located between FC and CI_{tetra} points on the S_1 potential energy surface (PES). The electronic structure changes at CI_{tetra} could be reasonably explained by this mechanism, because it has been well documented that the $\pi \rightarrow \pi^*$ double excitation configuration in the S_1 state of CBD becomes the major component in the ground state electronic wave function of THD.[23−25,27] However, there are at least two questions yet to be answered. First, experimentally, two absorptions had been observed for CBD derivatives, with one strong absorption centered at ca. 300 nm and a weak band at >400 nm. Although both of them were assigned to optically allowed 1^B_1 states,[14,18,19] the electronic character of both states has not been well elucidated. Second, this mechanism did not explain the easily observed dissociation channel. Actually, $\pi \rightarrow \pi^*$ single excitation could only weaken the π bonds, whereas C−C bond cleavage is expected to take place upon σ bond excitation.

To answer these questions, it is necessary to recompute the vertical excitation energies using high-level ab initio methods, which include adequate description of both nondynamical and dynamical correlations. On the other hand, the $\sigma \rightarrow \pi^*$ characterized S_3 state (2^1B_1 state at FC point) should be included in addition to S_1 and S_2 states in order to understand the dissociation path. For TMS-CBD, our calculations will show that the most intensive absorption near 300 nm should be assigned to S_3 state rather than S_1 state. On the basis of the $S_0 \rightarrow S_3$ FC excitation, we would suggest an alternative mechanism which could provide a consistent explanation on both reaction channels. Information about the geometrical and electronic properties of the critical points including minimum points and conical intersections on relevant potential energy surfaces will be presented with detailed analyses. Relations among these stationary points will be discussed with emphases on their importance in helping us understand the experimental findings.[18,28]

COMPUTATIONAL DETAILS

Because the D_2 group symmetry is maintained in all the minimum point geometries of relevant states, we use its irreducible representation labels A and B_1 to indicate the symmetry of the electronic states. However, along the reaction coordinates, in-plane and out-of-plane distortions can break the D_2 symmetry. Accordingly, we use the adiabatic state labels (S_n) when referring to state transitions.

Potential energy surface crossings among several lower-lying excited states as well as the ground state are calculated at the level of complete active space self-consistent field (CASSCF),[29,30] spanned with 12 electrons distributed in four π orbitals and eight σ orbitals on the CBD core, which ensures a reliable computation of the nondynamical electron correlation both in the CBD to THD isomerization process and in the dissociation process of the CBD core. The critical points on the potential energy surfaces, including equilibrium geometries of the ground and excited states are optimized with the state-averaged CASSCF method. The minimum energy conical intersection (MECI, hereafter abbreviated as "conical intersection") points are optimized following Robb's strategy.[31] To investigate the effect of dynamic correlation on excitation energies, single-point calculations are also performed with the equation-of-motion coupled-cluster model with single and double excitations (EOM-CCSD)[32] as well as the Multi-Reference Møller−Plesset (MRMP)[33,34] methods for some characteristic geometries on the potential energy surfaces. MRMP calculations are performed on the reference function obtained with a state-averaged CASSCF-(12,12) calculation including four lowest singlet states. Although the EOM-CCSD method is a highly recommended method for computing excitation energies within the single reference framework, the computational error is found to be quite too large for the doubly excited S_2 state of CBD. For systems like CBD, whose target states are multiconfigurational due to orbital degeneracies, the reference state should be chosen as a high-spin state, and the low-spin state could be obtained by the spin-flip EOM operators (EOM-SF models).[35] Furthermore, for a better description of the double-excitation character in the S_2 state of

CBD, one needs to expand the configuration interaction basis set for the similarity-transformed Hamiltonian; however, it is presently too time-consuming and storage-demanding for systems as large as TMS-CBD.

Implementation of the mixed basis (MixB) set has been shown to be very effective in cutting down the computational cost without serious loss of accuracy in computing CBD derivatives with tetra-*tert*-butyl substituents.[26] In this work, this strategy is employed by combining the 6-31G(d) basis set[36−40] (for the atoms on the CBD core) and STO-3G basis set[41,42] (for the atoms on the substituents). However, the full 6-31G(d) basis set is employed in computing the ground state geometry as well as the vertical excitation energies.

Density functional theory (DFT) calculations using the B3LYP functional[43−46] are performed using GAUSSIAN package.[47] Although the MOLPRO package is used for CASSCF and EOM-CCSD calculations,[48] GAMESS package is for MRMP calculations.[49,50]

■ RESULTS AND DISCUSSION

Franck−Condon Excitation. To elucidate the mechanism of the photochemical process starting from TMS-CBD, we begin with the study of the Franck−Condon excitation. The geometry optimization at the level of B3LYP/6-31G(d) indicates a ground state structure of D_2 symmetry, in which the CBD core is slightly distorted from the planar conformation.

Because the following multireference calculations are performed with natural orbitals obtained from a preceding CASSCF calculation, detailed analysis of the natural orbitals that are involved deeply in FC excitation, as well as in succeeding reaction steps, is helpful in understanding the evolution of electronic wave function along each reaction channel. In Figure 1, we illustrate two π-type natural orbitals 94 (π_S) and 95 (π_L), and one σ-type natural orbital 93 (σ_L). Obviously, orbitals 94 and 95 have a nodal plane perpendicular to the CBD moiety, bisecting the two longer or shorter bonds, respectively, similar to the Hartree−Fock HOMO or LUMO molecular orbitals. Orbital 93 is located on the two longer bonds, which indicates that it could be easily excited. It is worth noticing that all of these frontier orbitals are essentially composed of the atomic orbitals in the CBD core, which implies that the bulky substituents should mostly affect the FC excitations through the dynamical correlation instead of the static correlation.

On the basis of these orbitals, the three lowest excited states are analyzed, with the major components in the wave functions as well as the oscillator strengths collected in Figure 1. In sequence of excitation energy, S_1 is the first optically allowed excited state of B_1 symmetry, characterized as $\pi_S \rightarrow \pi_L$ single excitation, with a small oscillator strength; S_2 (2^1A) is the first optically forbidden state with predominant $\pi_S^2 \rightarrow \pi_L^2$ double-electron excitation. The excitation characters of S_1 and S_2 are similar to those of unsubstituted CBD, which were calculated with EOM-SF-CCSD and multireference average-quadratic coupled cluster (MR-AQCC) methods.[35,51] Above them, S_3 (2^1B_1) is again optically allowed with a much larger oscillator strength than S_1 and is dominated by $\sigma_L \rightarrow \pi_L$ single excitation.

To evaluate the effect of the dynamical electronic correlation, against the CASSCF results, we list in Table 1 the vertical excitation energies computed with several high-level ab initio methods including EOM-CCSD and MRMP, which are expected to agree better with the experimental observations. It could be seen that CASSCF results compare well with MRMP ones in predicting the excitation energy of S_2 state; the disagreements

Table 1. Vertical Excitation Energies of the Three Lowest Excited States at the Ground State Equilibrium Geometry[a]

method	ΔE_{S_1-GS} (eV)	ΔE_{S_2-GS} (eV)	ΔE_{S_3-GS} (eV)
CASSCF(12,12)/MixB	3.64	3.99	5.22
CASSCF(12,12)/6-31G(d)	3.48	3.76	5.02
MRMP(12,12)/MixB	3.07	3.80	4.31
EOM-CCSD/MixB	3.13	-	4.10
EOM-CCSD/6-31G(d)	2.95	-	3.99
exptl	$2.74^b (2.68)^c$	-	$3.44^{b,d} (3.98)^c$

[a]Ground-state equilibrium geometry is optimized with B3LYP/6-31G(d) method. [b]Obtained from UV−vis spectroscopy of TMS-CBD in hexane.[18] [c]From UV−vis spectroscopy of perfluoroaryltetrahedranes in hexane.[19] [d]This was originally reported as 226 nm (5.49 eV) in ref 18 and has been corrected with confirmation from the author through a private communication.

among CASSCF, MRMP, and EOM-CCSD results are around 0.5 eV for S_1 state; however, for the S_3 state, the excitation energy is more than 1 eV overestimated by CASSCF in comparison with the results from MRMP and EOM-CCSD calculations. It is not difficult to understand the unbalanced accuracy of CASSCF method in computing different electronic states. With all π and σ electrons in the CBD core included in the active space, the $\sigma-\pi$ polarization effect can be addressed satisfactorily in computing both S_1 and S_2 states, which are characterized as $\pi \rightarrow \pi^*$ excitations. On the other hand, the S_3 state corresponds to the $\sigma \rightarrow \pi^*$ excitation, where dynamical electronic correlation between the CBD core and the attached bulky groups should be included. Hence, for a reliable prediction of the excitation energies for different electronic states of TMS-CBD, a balanced treatment of $\sigma-\pi$ as well as $\pi-\pi$ electronic interactions is necessary. Similar to the previous study of unsubstituted CBD, the EOM-CCSD method could still present qualitatively correct excitation energies for singly excited S_1 and S_3 states, even though the ground state of TMS-CBD is substantially multiconfigurational.[35]

We note that the EOM-CCSD method predicts the vertical excitation energies to be around 3.99 eV (~310 nm) and 2.95 eV (~420 nm) for S_3 and S_1 states, respectively. Since the S_3 state is located above the S_1 state and presents a much greater oscillator strength, we could reasonably assign the S_3 state to the stronger absorption peak experimentally observed at 311 nm,[18] while S_1 state to the much weaker band around 462 nm, in contrast with the study of tetra-*tert*-butyl substituted CBD, where the main absorption at approximately 300 nm is assigned to S_1 state.[24,25] Considering the experimental findings where a UV irradiation with low-pressure mercury lamp (254 nm) is applied,[18] the photoinduced isomerization process of TMS-CBD could be initiated from both S_1 and S_3 states.

In the next section, we will show that upon the $S_0 \rightarrow S_3$ excitation, in addition to the isomerization channel connected to TMS-THD, the dissociation channel could also be opened after passing through one S_3/S_2 conical intersection.

Mechanism for Photoreactions. Locating various critical points on relevant potential energy surfaces could be very helpful in understanding the mechanism of photochemical reactions. These critical points include the minimum points on the PES of relevant states, as well as the conical intersections between PES's along possible reaction paths. In this section, characteristic geometrical parameters of minimum points are tabulated in Table 2, and those of CI points can be found in Figures 2, 4, and

Table 2. Characteristic Geometrical Parameters of the Minimum Points on Low-Lying Electronic States for TMS-CBD, Which Are Calculated with the CASSCF(12,12)/MixB Method

	$(1^1A)_{min}$	$(2^1A)_{min}$	$(1^1B_1)_{min}$	$(2^1B_1)_{min}$
	(S_0)	(S_1)	(S_2)	(S_3)
bond length (Å)				
C_1-C_3	1.621	1.490	1.475	1.674
C_1-C_2	1.387	1.490	1.475	1.376
C_1-Si	1.918	1.912	1.911	1.911
dihedral angle (deg)				
$C_1C_2C_4C_3$	4.8	5.1	5.5	1.3

5. The relative energies as well as the electronic characters of relevant states are presented in Scheme 2, Tables 3, 4, and Figure

Table 3. Major Components in the Electronic Wavefunctions of Low-Lying Excited States at the Equilibrium Geometries (D_2 Symmetry) Obtained at CASSCF(12,12)/MixB Level

	$(S_0)_{min}$	$(S_1)_{min}$	$(S_2)_{min}$	$(S_3)_{min}$
1^1A	$(\pi_S)^2(\pi_L)^0$	$(\pi_S)^2(\pi_L)^0$	$(\pi_S)^2(\pi_L)^0$	$(\pi_S)^2(\pi_L)^0$
	82.4%	44.0%	44.3%	83.7%
		$(\pi_S)^0(\pi_L)^2$	$(\pi_S)^0(\pi_L)^2$	
		44.0%	44.2%	
2^1A	$(\pi_S)^0(\pi_L)^2$	$(\pi_S)^2(\pi_L)^0$	$(\pi_S)^2(\pi_L)^0$	$(\pi_S)^0(\pi_L)^2$
	76.0%	41.4%	41.8%	75.0%
		$(\pi_S)^0(\pi_L)^2$	$(\pi_S)^0(\pi_L)^2$	
		41.4%	41.8%	
1^1B_1	$(\pi_S)^1(\pi_L)^1$	$(\pi_S)^1(\pi_L)^1$	$(\pi_S)^1(\pi_L)^1$	$(\pi_S)^1(\pi_L)^1$
	86.1%	90.2%	90.6%	83.3%
2^1B_1	$(\sigma_L)^1(\pi_L)^1$	$(\sigma_L)^1(\pi_L)^1$	$(\sigma_L)^1(\pi_L)^1$	$(\sigma_L)^1(\pi_L)^1$
	81.8%	43.1%	43.5%	80.8%
		$(\sigma_S)^1(\pi_S)^1$	$(\sigma_S)^1(\pi_S)^1$	
		43.1%	43.4%	

6. Cartesian coordinates, absolute energies, and major components of electronic configuration of all adiabatic states at all geometries are provided in the Supporting Information.

Minimum Points. As expected, the CBD skeleton of TMS-CBD presents alternating C—C bond lengths due to a pseudo-Jahn—Teller effect, which is similar to an unsubstituted CBD molecule.[4,52,53] Meanwhile, the electron-donating silyl groups increase the occupancy of the antibonding orbitals of the CBD core, which will further stretch the two longer C—C bonds by approximately 0.12 Å compared with the unsubstituted CBD.[52] Such a kind of bond length elongation can cancel out a large portion of the $\sigma_L \rightarrow \pi_L$ excitation energy by raising up the energy of σ_L orbital.

The geometrical character of S_1 state differs from that of S_0 state mainly in the equalized bond lengths on the CBD ring valued at 1.49 Å. This higher geometrical symmetry for the S_1

state could also be understood in view of the vibronic coupling between S_0 and S_1 states through a rectangular distortion mode, which could stabilize the S_0 state while destabilizing the S_1 state.[4,52,54] Accordingly, the CBD core distorts in a rectangular way in S_0 state, while maintaining its square geometry in the S_1 state. The electronic wave function of the S_1 state at its equilibrium geometry is characterized as the symmetrical combination of two degenerate configurations, $(\pi_S)^0(\pi_L)^2$ and $(\pi_S)^2(\pi_L)^0$, presenting A symmetry, as shown in Table 3. These two configurations are degenerate because the energy gap disappears between orbitals π_L and π_S due to the bond length equalization. At this geometry, the wave function of S_0 state is essentially an antisymmetrical combination of the above two configurations. The intensive mixing of the two configurations opens a gap between the two electronic states, which could subside on twisting the planar CBD ring to the pyramidal conformation, leading to a CI point between the S_1 and S_0 states.[24] Speaking of point group symmetry, the S_1 state at its own equilibrium geometry is correlated with the S_2 state at the ground-state equilibrium geometry.

At the minimum point of the S_2 PES, the bond lengths on the CBD ring are also equalized. The electronic wave function of this state is in B_1 symmetry, characterized as the $(\pi_S)^1(\pi_L)^1$ single excitation. It is obviously correlated with the S_1 state at the ground state equilibrium geometry, which implies that an S_1/S_2 conical intersection could be located at somewhere between the S_0 and S_2 (or S_1) PES minimum points. Further analysis of this crossing point will be presented later.

The electronic wave function of the S_3 state at its equilibrium geometry is in B_1 symmetry, attributed to the $\sigma_L \rightarrow \pi_L$ single excitation, which is unchanged with respect to the wave function at the FC region (see Table 3). By comparing the equilibrium geometries in S_0 and S_3 states, it could be found that the two longer bonds in the CBD core are stretched by approximately 0.05 Å, whereas the shorter bonds are slightly contracted by 0.01 Å in S_3 state. This point is particularly important because of its relevance to the dissociation process. By stretching the two longer C—C bonds, σ_L orbital energy is raised up to the frontier position, which manifests its essential role in the internal transition processes initiated from the S_3 state.

S_3/S_2 Conical Intersection. As shown in Figure 2 and Scheme 2, the S_3/S_2 CI point is labeled as CI_a. Starting from the FC point on the S_3 PES, going downhill to the minimum point, the CBD skeleton maintains its near-planar conformation, while the two longer C—C bonds are considerably stretched, and the two short ones slightly contracted. The CI_a point could be found at somewhere very close to the energy minimum on the S_3 PES, with less than 0.001 Å bond length deviations between these two structures. It is expected that an approach to this CI point should be straightforward upon an excitation to the S_3 PES.

The probability of an internal conversion through a CI point could be calculated as the scalar product of "derivative coupling

Table 4. Contribution of Major Electronic Configurations in Relevant States at Three Conical Intersections Calculated at CASSCF(12,12)/MixB Level

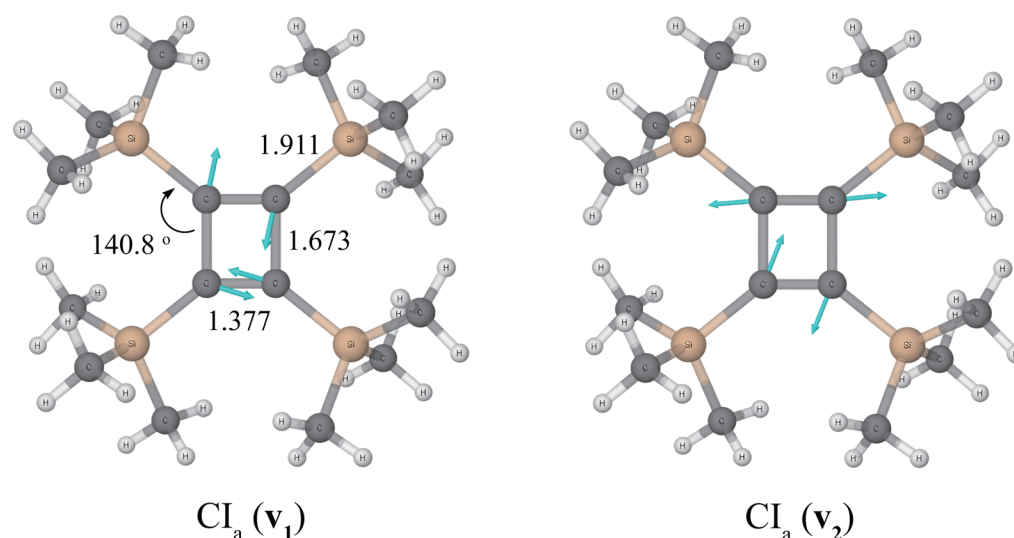| CI_a		CI_b		CI_c	
S_3	S_2	S_2	S_1	S_2	S_1
$(\sigma_L)^1(\pi_L)^1$	$(\sigma_L)^1(\pi_L)^1$	$(\sigma_L)^1(\pi_L)^1$	$(\sigma_L)^1(\pi_L)^1$	$(\pi_S)^0(\pi_L)^2$	$(\pi_S)^0(\pi_L)^2$
84.6%	<1.0%	53.8%	31.8%	73.4%	3.3%
$(\pi_S)^0(\pi_L)^2$	$(\pi_S)^0(\pi_L)^2$	$(\pi_S)^1(\pi_L)^1$	$(\pi_S)^1(\pi_L)^1$	$(\pi_S)^1(\pi_L)^1$	$(\pi_S)^1(\pi_L)^1$
<1.0%	75.5%	31.1%	52.9%	2.8%	86.9%

CI$_a$ (v$_1$)   CI$_a$ (v$_2$)

Figure 2. Geometry of TMS-CBD at S_3/S_2 conical intersection (CI$_a$) optimized at CASSCF(12,12)/MixB level, with the illustration of the derivative coupling vector $\mathbf{v}_1$ and the gradient difference vector $\mathbf{v}_2$.

Scheme 2. Schematic Energy Profile of the Potential Energy Surfaces of Four Low-Lying States along the Relaxation Coordinate[a]
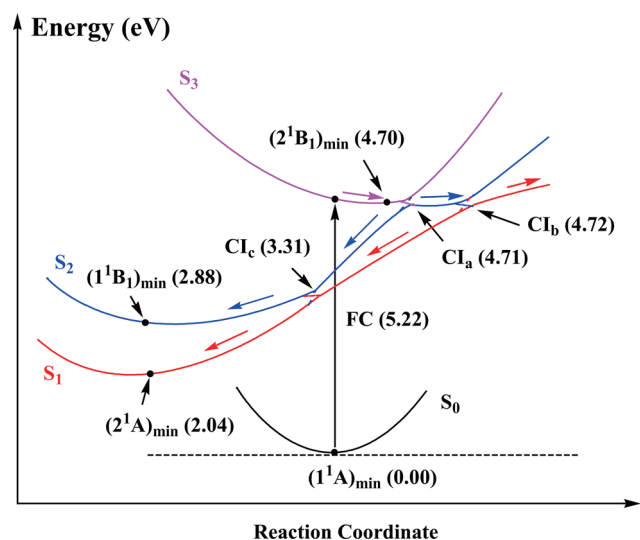
[a]The energies of critical points relative to the ground state energy are presented in brackets. The arrows indicate the possible relaxation paths via these CI points.

vector" of the two relevant electronic states and the velocity of nuclei[55]

$$d_{12} = \left\langle \psi_1 \left| \frac{\partial}{\partial \mathbf{R}} \psi_2 \right\rangle \cdot \mathbf{v} \right. \tag{1}$$

where $\mathbf{v} \equiv d\mathbf{R}/dt$ refers to the velocity of the nuclei, while the first term is the derivative coupling vector, which indicates the strength of the non-adiabatic coupling of the two crossing states. Although the derivative coupling vector of a CI point can be computed with the electronic wavefunctions of the two crossing states, the information on nuclear dynamics is only available from non-adiabatic dynamics simulations. Considering the vibronic coupling effect, the non-adiabatic transition could follow any directions in the branching plane of the CI point,[31,56] depending jointly on the directions of both the derivative coupling vector

and the nuclear velocity at the moment of state transition. Consequently, after passing through this CI point, two relaxation channels connecting to CI$_b$ and CI$_c$ respectively, will be opened, as shown in Scheme 2. The efficiency of the two channels can be evaluated through a statistical analysis of an ensemble of relaxation trajectories obtained from non-adiabatic dynamics simulations.

As has been discussed earlier, the dynamical correlation plays a critical role in the description of the S_3 state, for this reason we calculated the energy profile of relevant states along the interpolated path from the FC region to CI$_a$ with both CASSCF and MRMP methods. As shown in Figure 3, it could be found that the two potential energy surfaces at MRMP level may intersect at a lower energy region than is predicted with CASSCF method, this is due to the fact that the substituent effect, which plays a non-negligible role in further stabilizing the S_3 state, is accounted for as the dynamical correlation energy in MRMP treatment, while it is ignored in CASSCF calculations.

At a conical intersection, two vibrational modes can be defined, which will lift the degeneracy of the two states.[31] One is the previously mentioned derivative coupling vector $\mathbf{v}_1 = \langle \psi_i | (\partial/\partial \mathbf{R}) \psi_j \rangle$; the other is the gradient difference vector $\mathbf{v}_2 = \partial (E_i - E_j)/\partial \mathbf{R}$, where E_i and E_j are the upper and lower state energies, respectively. In Figure 2, we also present derivative coupling vector as well as the gradient difference vector at CI$_a$. Note that the combination of the two vectors at CI$_a$ point could generate two relaxation directions leading to either the dissociation of the CBD skeleton or the isomerization of it to THD structure.

S_2/S_1 Conical Intersections. Between the S_2 and S_1 potential energy surfaces, two CI points are located, which are labeled as CI$_b$ and CI$_c$, respectively, as shown in Figure 4. Let us take a look at one of the two crossing points, CI$_b$. After passing through the CI$_a$ point, along with the further stretching of the two longer C−C bonds, the S_2 state retains its major configuration of $\sigma_L \rightarrow \pi_L$ single excitation, which was inherited from the original S_3 state, whereas the S_1 state keeps its major configuration of $\pi_S \rightarrow \pi_L$ single excitation (see Table 4). Accordingly, the adiabatic wave functions of the two degenerate states at CI$_b$ should be constructed with these two major configurations, as shown in Table 4. In a specific nonadiabatic dynamics trajectory, the way of mixing of the two configurations is determined by the vibronic
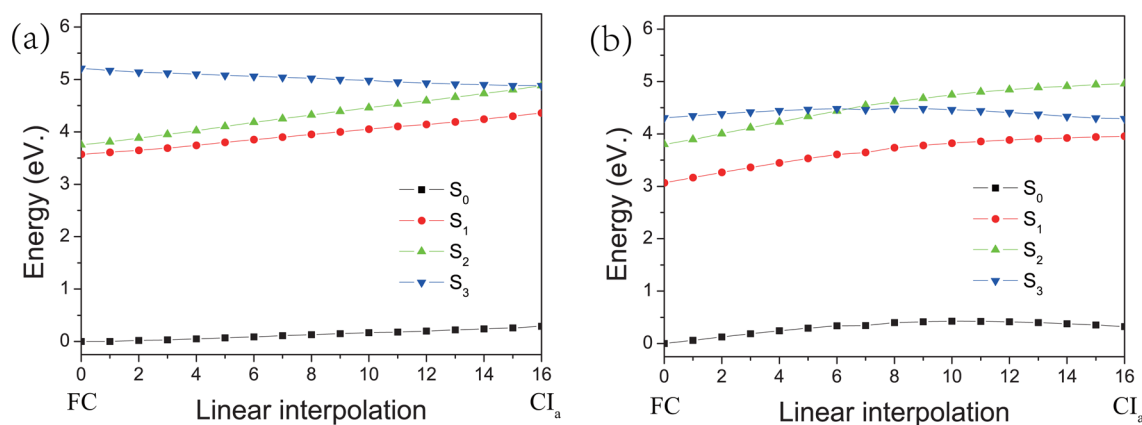
Figure 3. Energy profile of the relaxation path of S_3 state from the FC region to the S_3/S_2 conical intersection (CI$_a$): calculated at (a) CASSCF(12,12)/MixB level, (b) MRMP(12,12)/MixB level. The molecular geometries are derived by linear interpolations between FC and CI$_a$ geometries calculated with CASSCF(12,12)/MixB method.
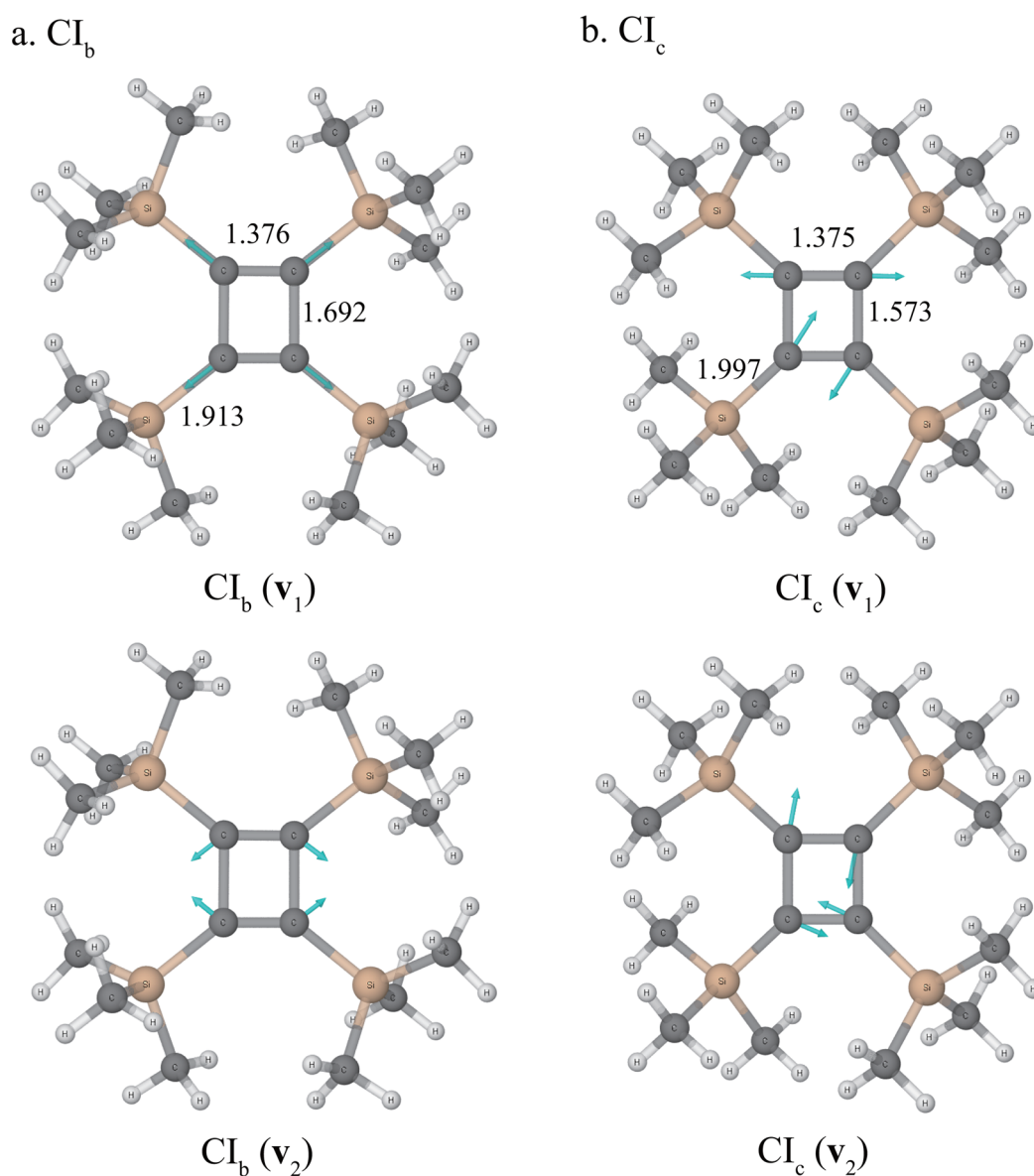

Figure 4. Geometries of TMS-CBD at S_2/S_1 CI points, (a) CI$_b$; (b) CI$_c$, optimized at CASSCF(12,12)/MixB level. The derivative coupling vector $\mathbf{v}_1$ and the gradient difference vector $\mathbf{v}_2$ are shown as well.
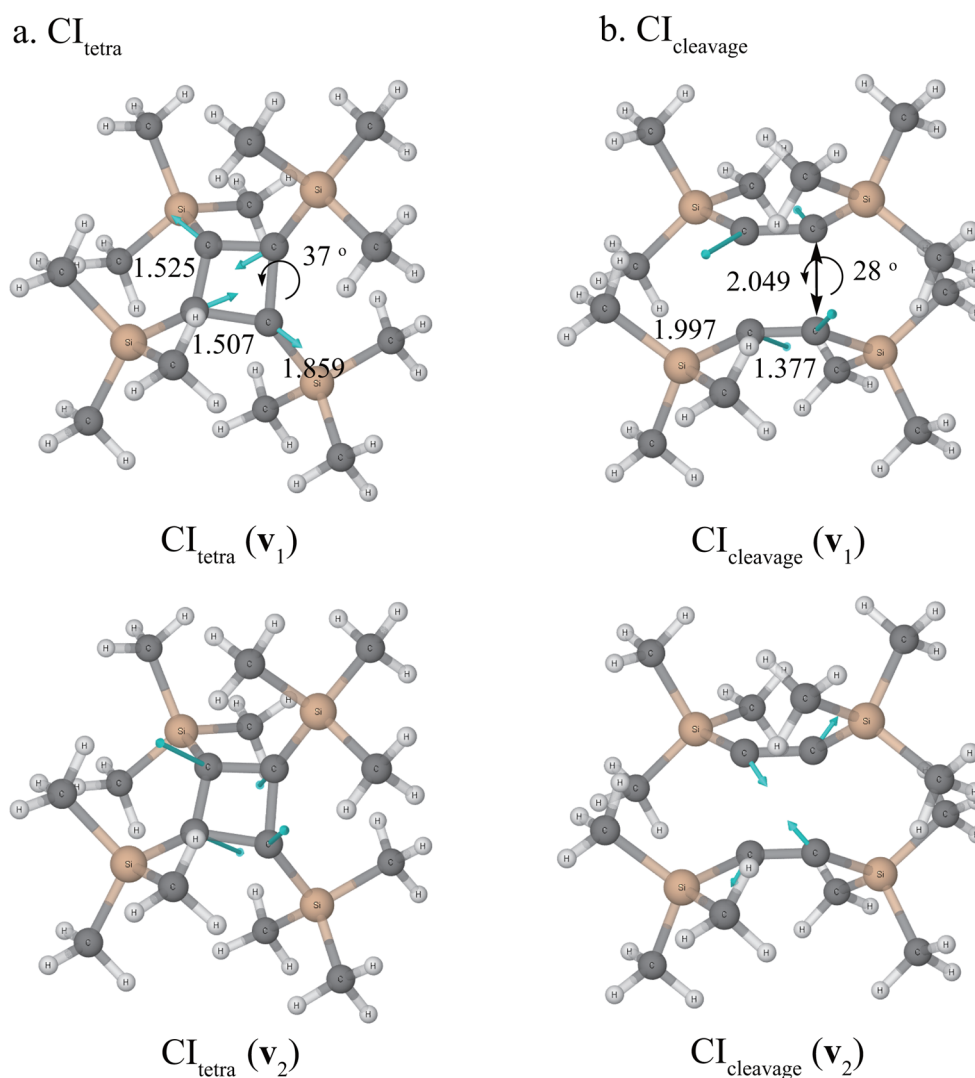
a. CI$_{tetra}$

b. CI$_{cleavage}$

CI$_{tetra}$ (**v**$_1$)

CI$_{cleavage}$ (**v**$_1$)

CI$_{tetra}$ (**v**$_2$)

CI$_{cleavage}$ (**v**$_2$)

Figure 5. Geometries of TMS-CBD at S_1/S_0 conical intersections, (a) CI$_{tetra}$; (b) CI$_{cleavage}$, optimized at CASSCF(12,12)/MixB level, as well as the derivative coupling vector **v**$_1$ and the gradient difference vector **v**$_2$.

coupling between the two relevant states, which opens two possible relaxation paths linking to the CI$_c$ and the CI$_{cleavage}$ (which will be discussed later), respectively. The way of geometrical transformation in the two relaxation paths after passing through CI$_b$ could be rationalized by exploring the two vectors CI$_b$ (**v**$_1$) and CI$_b$ (**v**$_2$). The sum of them defines a C−C bond breaking channel connected to two dissociated TMS-Ac molecules, whereas their difference defines a channel to CI$_c$, where the two longer C−C bonds in CBD skeleton are shortened.

CI$_c$ is another crossing point between the S_2 and S_1 potential energy surfaces, which is located beneath the CI$_b$. In principle, this CI point could be reached from both CI$_a$ and CI$_b$ via downhill relaxation pathways. Following these pathways, the longer C−C bond is considerably contracted by approximately 0.1 Å, resulting in significant stabilization of σ_L orbital. When arriving at the CI$_c$ point, the adiabatic wave functions of the two near-degenerate states S_2 and S_1 is composed of two character-istic configurations, $\pi_S \rightarrow \pi_L$ double excitation and $\pi_S \rightarrow \pi_L$ single excitation, which are inherited from the S_2 and S_1 states at the FC region, respectively, as shown in Table 4. Around this CI point, considering the vibronic coupling effect,[57,58] two relaxation paths should be opened, one to the S_2 minimum, the other to CI$_{tetra}$ (a

S_1/S_0 crossing point, which will be discussed shortly later). This could be helpful in understanding the 50% yield of conversion from TMS-CBD to TMS-THD upon a 70 h irradiation.[18] If the system moves on the S_2 PES toward the S_2 minimum point, the molecule could undergo transition to the ground state either through vibronic relaxation, whereas if it moves on S_1 PES, the isomerization process could be fulfilled by passing through CI$_{tetra}$. We note that similar isomerization processes were studied previously in CBD as well as its tetra-*tert*-butyl-substituted derivatives.[24−26]

A schematic energy profile of relevant electronic states along the relaxation paths is presented in Scheme 2, which is used to illustrate the relationship among the above-discussed critical points. It could be seen that, after FC excitation to S_3 state, the system follows a downhill path and quickly approaches the S_3/S_2 conical intersection point (CI$_a$), two decaying channels are followed afterward, linked to CI$_c$ by contracting the longer C−C bonds, and CI$_b$ through further stretching of the longer C−C bonds. Later, by passing through CI$_b$, two relaxation channels are opened toward either the dissociation of the CBD skeleton or the other S_2/S_1 conical intersection (CI$_c$). After CI$_c$, two relaxation paths leading to the S_2 minimum point and CI$_{tetra}$, respectively, are also proposed.
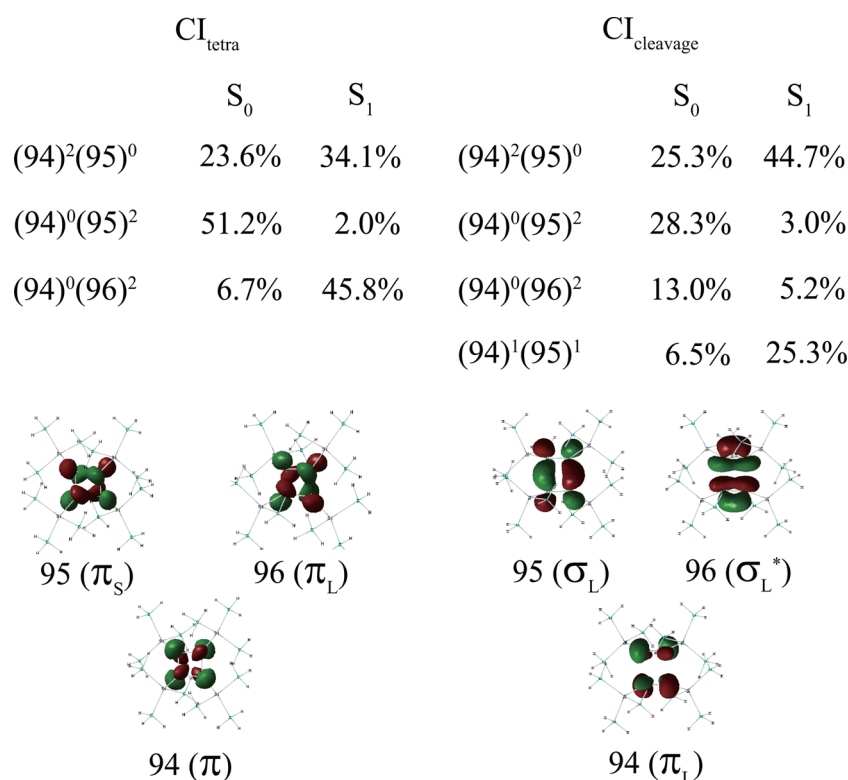
CI_{tetra}			$CI_{cleavage}$		
	S_0	S_1		S_0	S_1
$(94)^2(95)^0$	23.6%	34.1%	$(94)^2(95)^0$	25.3%	44.7%
$(94)^0(95)^2$	51.2%	2.0%	$(94)^0(95)^2$	28.3%	3.0%
$(94)^0(96)^2$	6.7%	45.8%	$(94)^0(96)^2$	13.0%	5.2%
			$(94)^1(95)^1$	6.5%	25.3%

$95\ (\pi_S)$ $96\ (\pi_L)$ $95\ (\sigma_L)$ $96\ (\sigma_L^*)$

$94\ (\pi)$ $94\ (\pi_L)$

Figure 6. Illustration of natural orbitals 94−96, and the contributions of major components in S_1 and S_0 wavefuntions at CI_{tetra} and $CI_{cleavage}$.

S_1/S_0 Conical Intersections. On the S_1 PES, two different S_1/S_0 CI points are found and presented in Figure 5. Following the previous study of tetra-*tert*-butyl CBD (TB-CBD), we label one of them as CI_{tetra}.[26] CI_{tetra}, with an energy of 2.6 eV above S_0 minimum of TMS-CBD, is connected to the TMS-THD minimum point on the S_0 PES, accordingly, its geometry could be regarded as an interpolation between CBD and THD. Roughly speaking, it deviates from the minimum point of the S_1 by lifting the atoms at two opposite corners away from the original CBD plane. At CI_{tetra}, the out-of-plane distortion leads to the hybridization of 2s and 2p atomic orbitals, which reduces the antibonding character in the original highest antibonding π orbital, and causes its energy to be lower than π_S and π_L. In this considerably stabilized orbital (labeled 94 in Figure 6), the four hybridized carbon atom orbitals located at four corners of the ring are weakly overlapped.

As shown in Figure 6, the adiabatic wave functions of S_1 and S_0 states share the same major component of $(94)^2(95)^0$ at CI_{tetra} point. Besides, S_1 has a predominant component of $(94)^0(96)^2$, whereas S_0 is characterized as $(94)^0(95)^2$. Due to near-equalization of the four C−C bonds in the CBD ring, orbitals 95 and 96 are nearly degenerate, which could also diminish the energy difference between $(94)^0(95)^2$ and $(94)^0(96)^2$ configurations, leading to the mutual approaching of S_0 and S_1 potential energy surfaces at CI_{tetra} point. The derivative coupling vector and gradient difference vector at CI_{tetra} are illustrated in Figure 5. Linear combination of the two vectors could generate a pyramidalization mode connecting to THD framework.

The other CI point, which is labeled $CI_{cleavage}$ with an energy of 4.2 eV above S_0 minimum of TMS-CBD, is connected to the dissociation products. Compared with CI_b, the longer C−C bonds are further stretched to 2.05 Å, the skeleton of the CBD ring is also distorted from the planar conformation as shown in Figure 5. Such geometrical change from CI_b to $CI_{cleavage}$

significantly weakens the atomic orbital overlap along the longer C−C bonds. As a result, the two σ type orbitals 95 and 96 with, respectively, considerable bonding and antibonding characters along the longer C−C bonds, present clearly nonbonding characters at the $CI_{cleavage}$ point and significantly take part in constructing both S_1 and S_0 wave functions. Orbital 94 (π_L) is the other most active orbital in the two states, which shows strong antibonding character on the shorter C−C bonds and weak bonding character on the longer ones.

As shown in Figure 6, at $CI_{cleavage}$, the adiabatic wave functions of both S_1 and S_0 states share the same major component of $(94)^2(95)^0$. Besides this common configuration, S_1 state has another major component of $(94)^1(95)^1$, which is inherited from the wave function at CI_b; however $(94)^0(95)^2$ configuration is the other major component in S_0 state, and this configuration is the predominant component in the ground state wave function of TMS-CBD at its equilibrium geometry. The derivative coupling vector and gradient difference vector at $CI_{cleavage}$ are illustrated in Figure 5. Combination of these two vectors could generate various vibrational modes, along one of which the TMS-CBD will dissociate into two TMS-Ac molecules.

After a detailed investigation of the critical points on relevant potential energy surfaces, a schematic diagram of the reaction mechanism is shown in Scheme 3. The photochemical processes of TMS-CBD isomerization and dissociation could be initiated from the FC excitation to the S_3 state. The total relaxation paths could be divided into two stages in terms of geometrical changes of the CBD skeleton. In the first stage, following a series of state transitions as well as geometrical relaxations from S_3 to S_1, the CBD skeleton approximately maintains its near-planar conformation. The second stage fulfills internal conversions from S_1 to S_0 via two nonplanar CI points, $CI_{cleavage}$ and CI_{tetra}, respectively. In summary, two relaxation channels leading to

Scheme 3. Schematic Diagram of the Photoreaction Paths for TMS-CBD through $\sigma - \pi^*$ Single Excitation[a]
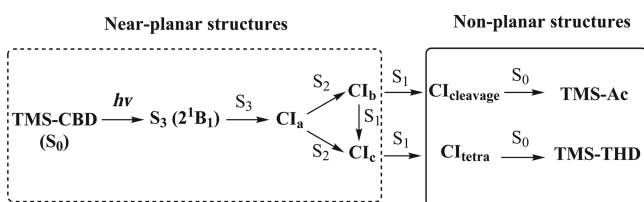
[a]The solid and dash arrows indicate the relaxation channels leading to TMS-Ac and TMS-THD, respectively.

the dissociation product (TMS-CBD) and the isomerization product (TMS-Ac), respectively, are described in Scheme 3.

We note that a static characterization of critical points on the potential energy surfaces could only supply the electronic coupling vectors at MECIs, whereas the efficiency of a radiationless internal conversion process is also dependent on the vector of nuclear momentum.[55] This point is particularly important for S_1/S_0 conversion process, where the vibronic relaxation could be a competitive process against the internal conversion discussed here, and this could be clarified by further nonadiabatic dynamics simulations.

CONCLUSION

The mechanism of the photochemical reaction in TMS-CBD has been investigated using the CASSCF method. The vertical excitation energies of several low-lying excited states are computed and compared using CASSCF, MRMP, and EOM-CCSD methods. Our calculations suggest that the Franck–Condon excitation most probably corresponds to the excitation to the second $^1B_1$ state (S_3), which is attributed to the $\sigma \rightarrow \pi$ single excitation, with an excitation energy available from low pressure mercury lamp irradiation.

The state transitions as well as geometrical relaxations in the excited states are discussed in detail by analyzing the minimum points as well as the conical intersections on relevant potential energy surfaces. Complete reaction channels have been suggested for the two major products, TMS-THD and TMS-Ac, which were reported experimentally. The first channel, which corresponds to the isomerization of the CBD skeleton to THD structure, is characterized by contracting the longer C–C bonds and via a tetra form conical intersection on S_2 PES. The other channel is attributed to the CBD skeleton dissociation, producing two TMS-Ac molecules. This dissociation channel takes place by further stretching of the longer C–C bonds after excitation into S_3 state, which makes it more competitive than the isomerization channel. These two possible relaxation paths can elucidate the mechanism of photochemical reactions of TMS-CBD upon irradiation of >300 nm.

Many CBD derivatives have been synthesized in the past decades, TMS-CBD is one of which showing unexpected thermodynamical stability at high temperatures, as well as fascinating photochemical behaviors. Thorough understanding of their physical and chemical properties requires careful treatment of the electronic effects of the substituent on chemical bonding in the CBD skeleton, with the dynamical electron correlations appropriately taken into consideration.

ASSOCIATED CONTENT

S **Supporting Information**

Details of the computational results, including absolute energies, electronic wave functions, as well as Cartesian coordinates of optimized structures have been collected in the Supporting Information. This material is available free of charge via the Internet at http://pubs.acs.org/.

AUTHOR INFORMATION

Corresponding Author

*E-mail: cgliu@nju.edu.cn. Phone: +86 (25) 83596756. Fax: +86 (25) 83596131.

Notes

The authors declare no competing financial interest.

ACKNOWLEDGMENTS

REFERENCES

(1) Emerson, G.; Watts, L.; Pettit, R. Cyclobutadiene- and benzocyclobutadiene- iron tricarbonyl complexes. *J. Am. Chem. Soc.* **1965**, *87*, 131−133.

(2) Bally, T.; Masamune, S. Cyclobutadiene. *Tetrahedron* **1980**, *36*, 343−370.

(3) Cram, D.; Tanner, M.; Thomas, R. The taming of cyclobutadiene. *Angew. Chem., Int. Ed. Engl.* **1991**, *30*, 1024−1027.

(4) Balková, A.; Bartlett, R. J. A multireference coupled-cluster study of the ground state and lowest excited states of cyclobutadiene. *J. Chem. Phys.* **1994**, *101*, 8972−8987.

(5) Deniz, A. A.; Peters, K. S.; Snyder, G. J. Experimental determination of the antiaromaticity of cyclobutadiene. *Science* **1999**, *286*, 1119−1122.

(6) Moran, D.; Manoharan, M.; Heine, T.; Schleyer, P. v. R. σ-Antiaromaticity in cyclobutane, cubane, and other molecules with saturated four-membered Rings. *Org. Lett.* **2003**, *5*, 23−26.

(7) Fattahi, A.; Lis, L.; Tian, Z.; Kass, S. R. The heat of formation of cyclobutadiene. *Angew. Chem., Int. Ed.* **2006**, *45*, 4984−4988.

(8) Bally, T. Cyclobutadiene: The antiaromatic paradigm? *Angew. Chem., Int. Ed.* **2006**, *45*, 6616−6619.

(9) Karadakov, P. B. Aromaticity and antiaromaticity in the low-lying electronic states of cyclooctatetraene. *J. Phys. Chem. A* **2008**, *112*, 12707−12713.

(10) Wu, J. I.-C.; Mo, Y.; Evangelista, F. A.; Schleyer, P. v. R. Is cyclobutadiene really highly destabilized by antiaromaticity? *Chem. Commun.* **2012**, *48*, 8437−8439.

(11) Maier, G. Tetrahedrane and cyclobutadiene. *Angew. Chem., Int. Ed. Engl.* **1988**, *27*, 309−332.

(12) Schleyer, P. v. R. Introduction: aromaticity. *Chem. Rev.* **2001**, *101*, 1115−1118.

(13) Schleyer, P. v. R. Introduction: delocalization-Pi and Sigma. *Chem. Rev.* **2005**, *105*, 3433−3435.

(14) Masamune, S.; Ona, H.; Suda, M.; Leichter, L. Cyclobutadiene. *J. Chem. Soc. Chem. Commun.* **1972**, *23*, 1268−1269.

(15) Sekiguchi, A.; Matsuo, T.; Watanabe, H. Synthesis and characterization of a cyclobutadiene dianion dilithium salt: Evidence for aromaticity. *J. Am. Chem. Soc.* **2000**, *122*, 5652−5653.

(16) Ishii, K.; Kobayashi, N.; Matsuo, T.; Tanaka, M.; Sekiguchi, A. Observation of the predicted negative faraday a MCD term in a cyclobutadiene dianion. *J. Am. Chem. Soc.* **2001**, *123*, 5356−5357.

(17) Maier, G.; Neudert, J.; Wolf, O. Tetrakis(trimethylsilyl)-cyclobutadiene and tetrakis (trimethylsilyl)tetrahedrane. *Angew. Chem., Int. Ed.* **2001**, *40*, 1674−1675.

(18) Maier, G.; Neudert, J.; Wolf, O.; Pappusch, D.; Sekiguchi, A.; Tanaka, M.; Matsuo, T. Tetrakis(trimethylsilyl)tetrahedrane. *J. Am. Chem. Soc.* **2002**, *124*, 13819−13826.

(19) Inagaki, Y.; Nakamoto, M.; Sekiguchi, A. Photoisomerization of perfluoroaryltetrahedranes to perfluoroarylcyclobutadienes. *J. Am. Chem. Soc.* **2011**, *133*, 16436−16439.

(20) Maier, G.; Pfriem, S.; Schäfer, U.; Matusch, R. Tetra-tert-butyltetrahedrane. *Angew. Chem., Int. Ed. Engl.* **1978**, *17*, 520−521.

(21) Maier, G.; Born, D. Tri-tert-butyl(trimethylsilyl)tricyclo-[1.1.0.0^{2,4}]-butane a second tetrahedrane derivative. *Angew. Chem., Int. Ed. Engl.* **1989**, *28*, 1050−1052.

(22) Kollmar, H. An MO theoretical study on the stability of tetrahedrane. *J. Am. Chem. Soc.* **1980**, *102*, 2617−2621.

(23) Kollmar, H.; Carrion, F.; Dewar, M. J. S.; Bingham, R. C. Ground states of molecules. 58. The C$_4$H$_4$ potential surface. *J. Am. Chem. Soc.* **1981**, *103*, 5292−5303.

(24) Sumita, M.; Saito, K. Ground state potential energy surface between cyclobutadiene and tetrahedrane looked down from S_1/S_0 conical intersections. *Tetrahedron* **2010**, *66*, 5212−5217.

(25) Sumita, M.; Saito, K. Tetra-radical and ionic S_1/S_0 conical intersections of cyclobutadiene. *Chem. Phys.* **2010**, *371*, 30−35.

(26) Sumita, M.; Saito, K.; Tateyama, Y. Computational study on photo- and thermo-reactions between tetra-tert-butyl-substituted cyclo-butadiene and tetrahedrane. *Comput. Theor. Chem.* **2011**, *969*, 44−52.

(27) Nemirowski, A.; Reisenauer, H. P.; Schreiner, P. R. Tetrahedrane-dossier of an unknown. *Chem.—Eur. J.* **2006**, *12*, 7411−7420.

(28) Arnold, B.; Michl, J. Ultraviolet and polarized infrared-spectroscopy of matrix-isolated cyclobutadiene and its isotopomers. *J. Phys. Chem.* **1993**, *97*, 13348−13354.

(29) Knowles, P. J.; Werner, H. J. An efficient second-order MCSCF method for long configuration expansions. *Chem. Phys. Lett.* **1985**, *115*, 259−267.

(30) Werner, H. J.; Knowles, P. J. A second order multiconfiguration SCF procedure with optimum convergence. *J. Chem. Phys.* **1985**, *82*, 5053−5063.

(31) Bearpark, M. J.; Robb, M. A.; Schlegel, H. B. A direct method for the location of the lowest energy point on a potential surface crossing. *Chem. Phys. Lett.* **1994**, *223*, 269−274.

(32) Korona, T.; Werner, H. J. Local treatment of electron excitations in the EOM-CCSD method. *J. Chem. Phys.* **2003**, *118*, 3006−3019.

(33) Nakano, H. Quasidegenerate perturbation theory with multi-configurational self-consistent-field reference functions. *J. Chem. Phys.* **1993**, *99*, 7983−7992.

(34) Witek, H. A.; Choe, Y. K.; Finley, J. P.; Hirao, K. Intruder state avoidance multireference Møller−Plesset perturbation theory. *J. Comput. Chem.* **2002**, *23*, 957−965.

(35) Levchenko, S.; Krylov, A. Equation-of-motion spin-flip coupled-cluster model with single and double substitutions: Theory and application to cyclobutadiene. *J. Chem. Phys.* **2004**, *120*, 175−185.

(36) Hehre, W. J.; Ditchfield, R.; Pople, J. A. Self-consistent molecular-orbital methods 0.12. further extensions of gaussian-type basis sets for use in molecular-orbital studies of organic-molecules. *J. Chem. Phys.* **1972**, *56*, 2257−2261.

(37) Hariharan, P. C.; Pople, J. A. Influence of polarization functions on molecular-orbital hydrogenation energies. *Theor. Chem. Acc.* **1973**, *28*, 213−222.

(38) Hariharan, P. C.; Pople, J. A. Accuracy of AH$_n$ equilibrium geometries by single determinant molecular-orbital theory. *Mol. Phys.* **1974**, *27*, 209−214.

(39) Gordon, M. S. The isomers of silacyclopropane. *Chem. Phys. Lett.* **1980**, *76*, 163−168.

(40) Francl, M. M.; Pietro, W. J.; Hehre, W. J.; Binkley, J. S.; Gordon, M. S.; DeFrees, D. J.; Pople, J. A. Self-consistent molecular-orbital methods 0.23. A polarization-type basis set for second-row elements. *J. Chem. Phys.* **1982**, *77*, 3654−3665.

(41) Hehre, W. J.; Stewart, R. F.; Pople, J. A. Self-consistent molecular-orbital methods.I. use of gaussian expansions of Slater-type atomic orbitals. *J. Chem. Phys.* **1969**, *51*, 2657−2664.

(42) Collins, J. B.; von R. Schleyer, P.; Binkley, J. S.; Pople, J. A. Self-consistent molecular orbital methods. XVII. Geometries and binding energies of second-row molecules. A comparison of three basis sets. *J. Chem. Phys.* **1976**, *64*, 5142−5151.

(43) Becke, A. D. Density-functional exchange-energy approximation with correct asymptotic-behavior. *Phys. Rev. A* **1988**, *38*, 3098−3100.

(44) Lee, C. T.; Yang, W. T.; Parr, R. G. Development of the Colle-Salvetti correlation-energy formula into a functional of the electron-density. *Phys. Rev. B* **1988**, *37*, 785−789.

(45) Becke, A. D. Density-functional Thermochemistry 0.3. the Role of exact exchange. *J. Chem. Phys.* **1993**, *98*, 5648−5652.

(46) Stephens, P. J.; Devlin, F. J.; Chabalowski, C. F.; Frisch, M. J. Ab initio calculation of vibrational absorption and circular dichroism apectra using density functional force fields. *J. Phys. Chem.* **1994**, *98*, 11623−11627.

(47) Frisch, M. J. ; Trucks, G. W.; Schlegel, H. B. ; Scuseria, G. E. ; Robb, M. A. ; Cheeseman, J. R. ; Scalmani, G. ; Barone, V. ; Mennucci, B. ; Petersson, G. A. et al. *Gaussian 09*, revision B.01, Gaussian, Inc.: Wallingford CT, 2010.

(48) Werner, H.-J.; Knowles, P. J.; Lindh, R.; Manby, F. R.; Schütz, M.; Celani, P.; Korona, T.; Rauhut, G.; Amos, R. D.; Bernhardsson, A. et al. *MOLPRO*, version 2010.1, a package of *ab initio* programs, see http://www.molpro.net.

(49) Schmidt, M. W.; Baldridge, K. K.; Boatz, J. A.; Elbert, S. T.; Gordon, M. S.; Jensen, J. H.; Koseki, S.; Matsunaga, N.; Nguyen, K. A.; Su, S.; Windus, T. L.; Dupuis, M.; Montgomery, J. A. General atomic and molecular electronic structure system. *J. Comput. Chem.* **1993**, *14*, 1347−1363.

(50) Gordon, M. S.; Schmidt, M. W. In *Theory and Applications of Computational Chemistry*; Dykstra, C. E., Frenking, G., Kim, K. S., Scuseria, G. E., Eds.; Elsevier: Amsterdam, 2005; pp 1167 − 1189.

(51) Eckert-Maksić, M.; Vazdar, M.; Barbatti, M.; Lischka, H.; Maksić, Z. B. Automerization reaction of cyclobutadiene and its barrier height: An ab initio benchmark multireference average-quadratic coupled cluster study. *J. Chem. Phys.* **2006**, *125*, 064310.

(52) Nakamura, K.; Osamura, Y.; Iwata, S. Second-order Jahn−Teller effect of cyclobutadiene in low-lying states. An MCSCF study. *Chem. Phys.* **1989**, *136*, 67−77.

(53) Sancho-García, J. C.; Pittner, J.; Čársky, P.; Hubač, I. Multireference coupled-cluster calculations on the energy of activation in the automerization of cyclobutadiene: Assessment of the state-specific multireference Brillouin-Wigner theory. *J. Chem. Phys.* **2000**, *112*, 8785−8788.

(54) Borden, W. T.; Davidson, E. R. Theoretical studies of diradicals containing four π electrons. *Acc. Chem. Res.* **1981**, *14*, 69−76.

(55) Tully, J. C. Molecular-dynamics with electronic-transitions. *J. Chem. Phys.* **1990**, *93*, 1061−1071.

(56) Celani, P.; Robb, M. R.; Garavelli, M.; Bemardi, F.; Olivucci, M. Geometry optimization on a hypersphere. Application to finding reaction paths from a conical intersection. *Chem. Phys. Lett.* **1995**, *243*, 1−8.

(57) Woywod, C.; Domcke, W.; Sobolewski, A.; Werner, H. Characterization of the S_1-S_2 conical intersection in pyrazine using ab initio multiconfiguration self-consistent-field and multireference configuration-interaction methods. *J. Chem. Phys.* **1994**, *100*, 1400−1413.

(58) Kühl, A.; Domcke, W. Multilevel Redfield description of the dissipative dynamics at conical intersections. *J. Chem. Phys.* **2002**, *116*, 263−274.